Adaptive tracking of the Barents Sea polar front using an autonomous underwater vehicle

Tore Mo-Bjørkelund[*], Eivind Kolås[2], Ilker Fer[2,3], and Martin Ludvigsen[1,4]

[1]Department of Marine Technology, Norwegian University of Science and Technology, Trondheim, Norway
[2]Geophysical Institute, University of Bergen and Bjerknes Centre for Climate Research, Bergen, Norway
[3]
[4]Arctic Geophysics Department, University Centre in Svalbard (UNIS), Longyearbyen, Norway
[5]Arctic Technology Department, University Centre in Svalbard (UNIS), Longyearbyen, Norway

Abstract

Exchanges and interactions between water masses are typically concentrated across ocean fronts, requiring targeted sampling. As fronts are dynamic in their spatiotemporal extent they can be hard to map with limited sampling resources. In this paper, we use horizontal temperature gradient as the defining feature of a front to adapt the path of an autonomous underwater vehicle to follow these regions of scientific interest. We present results from simulations and successful field operations in the Barents Sea, where the vehicle equipped with a microstructure sensor crossed the polar front while adapting its trajectory to the front position. Using in situ measurements, we estimate the temperature gradient across the polar front and cross it at different depths. We show that the vehicle is able to estimate and detect the temperature gradient maximum and to adjust its path to provide measurements of temperature, salinity and microstructure along its path, on both sides of the front. This is a step towards the integration of turbulence measurements on autonomous underwater vehicles, showing promise of more targeted sampling of turbulence in regions of large spatial gradients and interactions between water masses, such as fronts. The horizontal vehicle path complements the more traditional vertical profile measurements, providing a finer horizontal spatial resolution. The adaptive behavior of autonomous agents contributes to increased accuracy in targeted measurements as well as expanded resource utilization.

Keywords: Autonomous underwater vehicles, Turbulence, Temperature gradients, Adaptive sampling, Front, Barents Sea, Planning

1 Introduction

Ocean fronts are boundaries between distinct water masses, and are characterized by horizontal gradients. The water masses may differ in temperature, salinity, density and nutrient content, making them separable by measuring these variables (Belkin et al., 2009). The frontal region is associated with increased turbulence and energy dissipation compared to the open ocean, where the increased turbulence act to weaken the horizontal gradient, mixing the interacting water masses (D'Asaro et al., 2011). This interaction across fronts is important for physical, biogeochemical and biological variables, and usually a driver for life and activity. In our region of interest, the north-western Barents Sea (Fig. 2a), the polar front is a thermo-haline front between the Atlantic water carried by the Norwegian current and the Arctic waters and sea

---

[*]Corresponding author, email: `tore.mo-bjorkelund@ntnu.no`

ice present further north (Oziel et al., 2016). Here, the warmer, saltier Atlantic water meets the colder, fresher Arctic water along a topographically constrained front between the Spitsbergen Bank and the Great Bank (Gawarkiewicz and Plueddemann, 1995; Parsons et al., 1996). Understanding the dynamics across this front, and the processes maintaining and homogenizing the gradients, is important for quantifying the heat exchange between the Atlantic and Polar waters, and the effects of Atlantic water intruding into the Barents Sea.

The advent of the Autonomous Underwater Vehicle (AUV) has enabled ocean scientists to capture data more efficiently and concurrently. Adaptive behaviour in AUVs has been a field of study steadily increasing in the past decades, where the targeted sampling of specific phenomena has been the goal. Methods presented in Zhang et al. (2012, 2013, 2016) used adaptive behaviour and modelling to identify and sample a stratified, upwelling front and upwelled waters, whereas Fossum et al. (2021a) presented a method for crossing a temperature front. Zhang et al. (2019) used adaptive behaviour to keep an AUV along the isotherm associated with the deep chlorophyll-a maximum, acting as a pseudo-Lagrangian drifter. The on-board planner, Teleo-Reactive Executive software (T-REX, McGann et al. (2008)) has been used in the past decade for tracking chlorophyll-a maxima (Fossum et al., 2019; Fossum, 2019) and river plume boundaries (Fossum et al., 2021b), running the software on board a Light AUV (LAUV) (Sousa et al., 2012). Pinto et al. (2018) present the use of multiple AUVs, informed by aerial drones and remote sensing to track and map the outline of the Douro river plume outside Porto, Portugal. Hypoxic river regions were found and sampled adaptively by Stankiewicz et al. (2021). Subsumption based front crossing algorithms are presented in Fossum et al. (2021a); Zhang et al. (2012, 2013, 2016), where they estimate whether the front is crossed or not, implicitly determining the front location. In this paper we present a method for ocean front detection and crossing using an AUV, explicitly determining the position of the front, defined as the position of maximal horizontal temperature change. Our goal is to show that this method is suitable for detecting and tracking a front at specific, consecutive depths along one transect, with the expressed intention of gathering relevant microstructure data across an oceanic temperature front.

Collecting data with sufficient resolution to resolve the dissipation rate of turbulent kinetic energy across a front that varies in time and space is instrumentally demanding. In order to make such measurements in these dynamic regions of interest, targeted adaptive sampling can be done by autonomous agents carrying conductivity, temperature, depth and oceanic microstructure sensors. Microstructure sensors have previously been successfully integrated in robotic platforms such as gliders (Wolk et al., 2009b; Fer et al., 2014; Wolk et al., 2009a; Merckelbach et al., 2019), and Autonomous Underwater Vehicles (AUVs) such as REMUS (Goodman et al., 2006) and on the Autosub Long Range AUV (Garabato et al., 2019; Spingys et al., 2021). These efforts have shown the feasibility of integrating a microstructure sensor on an LAUV, developed at the Underwater Systems and Technology Laboratory at the University of Porto (Sousa et al., 2012).

2 Method

The method presented in this paper was developed as a tool for front detection and crossing at consecutive depths along a transect using temperature gradient as the defining factor of the front. It uses a sense-plan-act strategy (Seto, 2012; Fossum, 2019), in which underway measurements are used to determine the future trajectory of the sensor carrying platform. This method is specially designed for crossing temperature fronts, using an LAUV carrying a turbulence sensor package. To motivate the method presented we first describe the instruments used, followed by a presentation of the prerequisites and constraints informing the method design. Next we present the algorithm itself, followed by notes on the development and implementation.

2.1 Instrumentation

The method presented herein is designed to support the available technology; the LAUV and MicroRider-1000LP (MR) microstructure sensor from Rockland Scientific in Canada. The components and the method
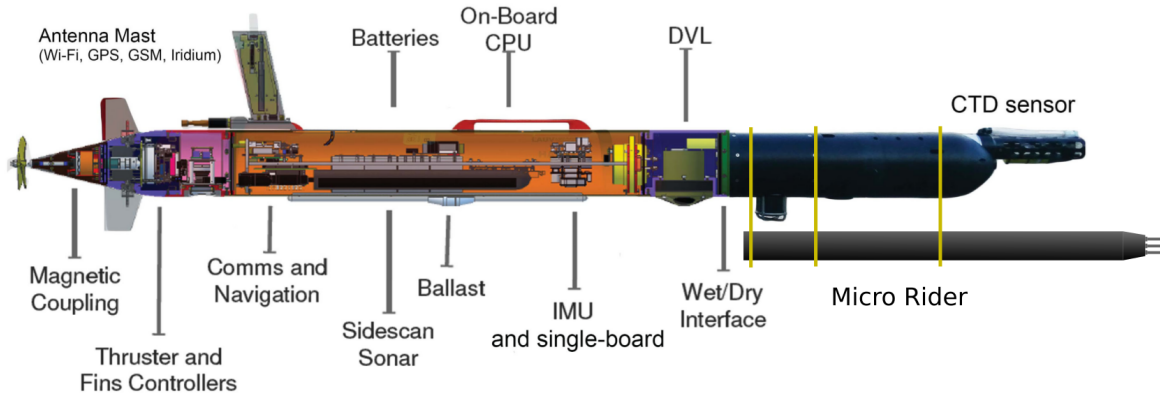
Figure 1: Overview of the AUV used for the experiment, LAUV Harald, with the MR, figure modified from Fossum et al. (2018).

were specifically targeted to achieve a robust adaptive front crossing, while delivering relevant and contextual data.

Light autonomous underwater vehicle

For the experiments, we used an LAUV, developed at the Underwater Systems and Technology Laboratory at the University of Porto, and commercially produced by OceanScan Marine Systems and Technology Lda. The vehicle, LAUV Harald, is owned by the Norwegian University of Science and Technology, and is equipped with the scientific payload of a SeaBird SBE FastCAT 49 conductivity, temperature and depth (CTD) sensor, a WetLabs EcoPuck Triplet fluorometer, and an Anderaa Optode 4831F dissolved oxygen sensor. The navigation package consists of a Nortek DVL1000, a GPS antenna, and a Lord Microstrain 3DM-GX4-25 Intertial Measurement Unit (IMU), as well as the on board software; DUNE: the Unified Navigation Environment (DUNE) (Sousa et al., 2012). Communication with the vehicle can be done over Wi-Fi, SMS/GSM, Iridium short burst data (SBD) and the on board Evologics S2CR 18/34 acoustic modem. LAUV Harald has two on board computers, one for the on board operating system, and one for user-defined tasks, termed *user-CPU*, see Figure 1 for placement of hardware.

Turbulence sensor package

The MR was first integrated and tested on LAUV Harald in May 2019, during a test cruise outside Ålesund, Norway, on board the RV Kristine Bonnevie. The MR was modified to the Tidal Energy (TE) configuration, earlier used in high flow tidal energy channels. The TE configuration includes increasing the sample rate to 1024 Hz for fast channels (from the typical 512 Hz). The increased sample rate allows reaching wavenumbers high enough to resolve the shear spectrum (reaching 164 cpm) at 1.2 m/s which is the operating speed of the LAUV in this study. For comparison, the typical operating speed of an ocean glider is 0.25 m/s, and the typical fall rate of vertical microstructure profilers is $0.5 - 0.8$ m/s.

The MR was attached beneath the LAUV, as indicated in Figure 1. It was powered by a stand alone lithium ion battery integrated in the vehicle, and controlled by a relay connected to the main power board inside the LAUV in order to provide a clean power source. Data was stored internally in the MR. The vertical axis-to-axis separation between the glider and the MR was approximately 30 cm. All turbulence sensors protruded about 25 cm from the nose of the AUV, outside the region of flow deformation. The MR was equipped with two airfoil velocity shear probes (SPM-38), a pressure transducer, a two-axis vibration sensor, and a high-accuracy dual-axis inclinometer. The MR samples the signal plus signal derivatives on the pressure transducer, and the derivative for shear signals, allowing high resolution measurements. For more details

about the MR and processing of the MR data from the field trial, the reader is referred to Kolås et al. (2022).

2.2 Prerequisites

The prerequisites for the method are the underlying assumptions and constraints, both of the vehicle used and in the scientific data collection. The prerequisites inform the method development and are vital to the motivation behind the design choices.

Assumptions

The method presented herein relies on five assumptions:

1. There is a horizontal correlation between the location of an ocean front at different depths.

2. The ocean process speed is slower than the vehicle speed.

3. The front can be approximated as a set of temperature measurements along a straight line with a known direction.

4. Prior knowledge is sufficiently good to make the trajectory cross the front.

5. The front location can be defined as the location of the maximum absolute value of the temperature gradient along a transect.

Assumption 1 is based on oceanographic knowledge of front systems (Oziel et al., 2016), and is used as an input when designing the method. In order for the front to be detected and revisited by the robot, Assumption 2 must hold, and from experience it usually does (Fossum, 2019), as the typical operating velocity of the LAUV is 1.2 m/s. Assumption 3 will hold if the robot does not travel along an isotherm and the sensing noise is less than the process signal. If the initial trajectory fails to cross or detect the intended front, the maximum gradient will be detected at some other point and may lead the adaptive mission astray. Thus, good prior information is needed, and we rely on assumption 4 to hold. Assumption 5 is used in estimating the front location.

Constraints

The large magnetic inclination at the high latitude resulted in high navigation drift rate and reduced accuracy of heading predictions, resulting in frequent surfacing for GNSS position measurements. Microstructure measurements impose additional constraints. For reliable dissipation estimates, shear probes must be exposed to flow past sensor with a small angle of attack within $\pm 20°$ (Osborn and Crawford, 1980). While slanted paths are possible on gliders (Fer et al., 2014), and AUVs (Fossum et al., 2021a; Zhang et al., 2016), we chose to use horizontal transects to adequately capture the horizontal gradient across the frontal system. Another constraint, is that the transect should be sufficiently longer than the typical front width. Limited by endurance, given the sharp front at site, we heuristically imposed 5km. This increases the chance of finding and crossing the front, as well as capturing the water masses on either side of the front, and making assumption 4 more likely to hold.

2.3 Front Detection and Crossing

Below we present the method for temperature gradient detection along a transect, and the adjustment of the ensuing transect in response to the measurements, capturing the front's greatest spatial change in temperature.

Natural Cubic Spline Regression

Along each transect, the temperature data is logged together with the vehicle position, these measurements get projected on to a line along the transect. In order to filter the temperature data, we use a natural cubic spline regression (NCSR). The spline is differentiable, and thus suitable for detecting gradients. NCSR is a method for fitting data to a set of cubic polynomials, defined over an interval of the input range, position along the transect in our case, with the constraint that their second order derivatives are continuous and zero at the ends. The partial NCSR function is denoted as:

$$S_i(x) = a_i + b_i x + c_i x^2 + d_i x^3 \qquad\qquad x \in [x_i, x_{i+1}] \qquad\qquad (1)$$

The full NCSR is then the collection of all $S_i(x)$ over the input domain, in our case this is the position along the transect, $[x_{min}, x_{max}]$; $S(x) = [S_0, S_1, \ldots, S_{n_k-1}]$, where n_k is the number of *knots*, or divisions between functions, in the spline. If the input data set has size m with $n_k = m$, the NCSR perfectly interpolates the data, and in the special case of $n_k = 0$, the NCSR reduces to a cubic polynomial regression with zero second derivatives at the ends. As the purpose of this NCSR is to filter the temperature data across the front along one axis, it has to have enough knots to capture the features in the data, while still filtering noise. From previous experience, $n_k = 6$ has proved to be sufficient for most ocean phenomena sampled along one dimension (Mo-Bjørkelund et al., 2020). This choice will smooth out any fine scale measurement and process noise, and enable us to capture the global feature of maximal gradient.

Inputs

Assumptions and prerequisites presented in section 2.2 have to be provided for the algorithm in order to achieve the goal of finding and tracking the temperature front. The algorithm needs the following inputs:

- Predicted front location, $[\text{lat}_0, \text{lon}_0]$.

- Front orientation, the predicted orientation of the front in relation to North, ψ.

- A list of the desired depths to explore, $\boldsymbol{d}$.

- The desired length of the front crossing transect, l.

- The desired speed for the vehicle, s_d.

- The low pass filter constant for location estimation, $\alpha \in [0, 1]$.

- The depth interval accepted in the data input for the front detection along a given transect, Δd, which excludes dive and ascent from the data set, leaving data gathered in the interval $d \pm \Delta d$.

- The number of knots in the spline regression for the front detector, n_k.

- The desired dive and ascent angle for the vehicle, θ_{dive}.

- The padding length, l_{pad}, for the transect, to account for transitory behavior when diving and ascending.

These inputs must be determined before starting the algorithm on the vehicle. The prior, $[\text{lat}_0, \text{lon}_0]$ and ψ, can be estimated from underway ship measurements and/or remote sensing, $\boldsymbol{d}$, l, s_d must be decided with operational and scientific constraints in mind, while α, Δd and n_k are tuning parameters. The first value of vector $\boldsymbol{d}$ must be the depth with the largest spatial correlation to the depth of the prior, and the consecutive depths should be as closely correlated as possible.

Algorithm 1: Front detection and crossing

\# initialization - load inputs;
$\mathbf{p}$ = generateInitialWaypoints([$\text{lat}_0, \text{lon}_0$], ψ, $\boldsymbol{d}[0]$);
for d *in* $\boldsymbol{d}$ **do**
  goToWp($\mathbf{p}$);
  data = collectDataAlongTransect();
  surface();
  data = filterData(data, Δd);
  [lat, lon] = detectMaximumGradientPosition(data, n_k);
  $\mathbf{p}$ = generateWaypoints([lat, lon], d, α, ψ);
end
goToWp($\mathbf{p}$);
surface();
exit();

Algorithm

We present the algorithm in Algorithm 1. The first step after loading the inputs is to generate the first set of waypoints, a set containing four waypoints, termed path $\mathbf{p}$. They are generated by using an Euclidean coordinate system, using [$\text{lat}_0, \text{lon}_0$] as the origin, aligning the x-axis with North, y-axis with East, and z-axis with Down. The waypoints are then converted to [lat, lon, z] using the m2deg-function, converting the lengths in meters to degrees in the appropriate direction. The horizontal plane waypoint generation is described in Equations (2-9).

$$\text{lat}_{wp_0} = \text{m2deg}(\cos(\psi) \cdot (l_{pad} + \frac{d}{\sin(\theta_{dive})} + \frac{l}{2})) + \text{lat}_0 \tag{2}$$

$$\text{lon}_{wp_0} = \text{m2deg}(\sin(\psi) \cdot (l_{pad} + \frac{d}{\sin(\theta_{dive})} + \frac{l}{2})) + \text{lon}_0 \tag{3}$$

$$\text{lat}_{wp_1} = \text{m2deg}(\cos(\psi) \cdot \frac{l}{2}) + \text{lat}_0 \tag{4}$$

$$\text{lon}_{wp_1} = \text{m2deg}(\sin(\psi) \cdot \frac{l}{2}) + \text{lon}_0 \tag{5}$$

$$\text{lat}_{wp_2} = \text{m2deg}(-\cos(\psi) \cdot \frac{l}{2}) + \text{lat}_0 \tag{6}$$

$$\text{lon}_{wp_2} = \text{m2deg}(-\sin(\psi) \cdot \frac{l}{2}) + \text{lon}_0 \tag{7}$$

$$\text{lat}_{wp_3} = \text{m2deg}(-\cos(\psi) \cdot (l_{pad} + \frac{d}{\sin(\theta_{dive})} + \frac{l}{2})) + \text{lat}_0 \tag{8}$$

$$\text{lon}_{wp_3} = \text{m2deg}(-\sin(\psi) \cdot (l_{pad} + \frac{d}{\sin(\theta_{dive})} + \frac{l}{2})) + \text{lon}_0 \tag{9}$$

The vertical waypoints are $\boldsymbol{z}_d = [z_{d_0}, z_{d_1}, z_{d_2}, z_{d_3}] = [0, d, d, 0]$. Together, these waypoints generate the path, for one transect, $\mathbf{p} = [wp_0, wp_1, wp_2, wp_3]$, where $wp_n = [\text{lat}_{wp_n}, \text{lon}_{wp_n}, z_{d_n}]$. Function $goToWp(\cdot)$ orders the vehicle to go to the four generated waypoints in consecutive order. The $collectDataAlongTransect$ function makes sure all temperature data gathered gets a corresponding position and depth attached to it, while the $filterData$ function removes data that is outside the boundary of $d \pm \Delta d$ removing the data from the decent and ascent, this data is then fed into $detectMaximumGradientPosition(\cdot)$. Here the data is aligned on one axis, along the transect, and a NCSR with n_k evenly spaced knots is performed. The regression is spatially differentiated and the location of the maximum or minimum, depending on the absolute value, spatial gradient is found. We then combine the previous estimate of the front location and the new estimate

using a discrete low pass filter, as presented in equation 10, where k is the index in the depth vector $\boldsymbol{d}$.

$$[\text{lat}_k, \text{lon}_k] = (1 - \alpha) \cdot [\text{lat}_{k-1}, \text{lon}_{k-1}] + \alpha \cdot [\text{lat}_{NCSR}, \text{lon}_{NCSR}] \tag{10}$$

2.4 Implementation

The implementation of the algorithm followed two separate steps; simulation and on board integration, concluding with field trials.

Simulation

As part of the development, a simulated vehicle and temperature field were used. The vehicle was simulated using the built in simulator in DUNE (Sousa et al., 2012). The temperature field was implemented as a simulated CTD sensor in DUNE, where the conductivity and temperature values were generated analytically based on the vehicle position and depth. Gaussian noise was added to the simulated measurements. The analytical expression for the simulated temperature was generated as:

$$T_{sim} = T_{base} + \Delta T \cdot S(l/l_f) + 0.5 \cdot d \cdot e^{-0.1d} + G_n \tag{11}$$

where T_{base} is the base temperature, ΔT is the temperature difference across the front, $S(\cdot)$ is the sigmoid function, l is the distance from the front, l_f is a constant determining the width of the front, and $G_n \sim \mathcal{N}(0, \sigma_n^2)$. With this simulator, we tuned the parameters T_{base}, ΔT, k, and σ_n in order to test front scenarios that resemble conditions found in the polar front. As the simulations were carried out to evaluate and implement the method, they had to be as closely linked to the field operation as possible, thus, the desired path of the vehicle, including surfacing events were also implemented in the simulations to test the logic.

Software

The method presented in Algorithm 1 was implemented on the LAUV Harald and set up to communicate with the on board operating system, via a TCP/IP connection. The algorithm was written in Python, and used the Robot Operating System (ROS) (Quigley et al., 2009) for communication, and interacted with the messaging system of DUNE, the Inter Module Communication API with a software bridge, implemented in C++.

Field Trials

The region of interest and the location for the field trials is the Barents Sea, shown on the map in Figure 2 a). On cruise, data from underway temperature measurements and vertical profiles are used to determine an opportune sampling location and front orientation. Based on these measurements, we set the transect length, desired depths and mission duration, making capturing the front more likely. A successful deployment was done during the Winter Process Cruise on board the research icebreaker RV Kronprins Haakon, 9 February to 1 March 2021 (Nilsen et al., 2021). In order to detect the prior surface front location, data from the on board Sea-Bird Electronics thermosalinograph, with water intake at 4 m depth was used. LAUV Harald was deployed at 07:30 on 26 February at 76°N 24.94′, 34°E 09.61′, and the prior surface front location was set to 76°N 25.27′,34°E 13.43′. The transect length was set to $l = 5000$ m, the depths were set to $\boldsymbol{d} = [10, 20, 30, 40, 50]$ m, the rotational speed of the propeller was set to 1500 RPM, the depth filtering was set to $\Delta d = 1.0$ m, the front orientation was set to $\theta = 90°$ (East-West), and the number of knots in the NCSR were set to $n_k = 6$.
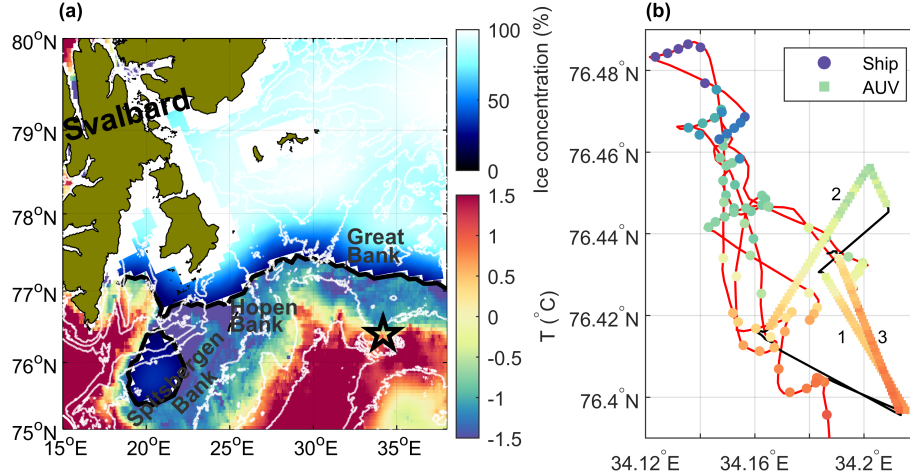
Figure 2: a) Overview map of the study region in the Barents Sea. White isobaths are drawn at 100, 200, 300 and 500 m depth using IBCAO-v4 (Jakobsson et al., 2020). Ice concentration and ice edge (thick black contour) on 26 February 2021 is from OSI SAF (OSI SAF, 2017). Sea surface temperature is from the product SEAICE_ARC_SEAICE_L4_NRT_OBSERVATIONS_011_008 at 0.05° resolution based upon observations from the Metop_A AVHRR instrument. Experiment location marked by a star near 34°E is expanded in b). b) Ship's track (red) with near-surface temperature from the ship's thermosalinograph, and AUV's track (black) with AUV's temperature measurements along the three transects are color coded (temperature color scale is the same as in panel a).

3   Results

3.1   Simulation

Here we show the results of one of the simulations carried out in the course of the development of the algorithm. The front in this case is simulated to be aligned with the North-South axis, and thus the AUV path is along the East-West axis. The entire simulated transect, temperature and estimated front positions are plotted in Figure 3, where the surfacing between each transect is visible. The front was simulated to have a nominal horizontal extent (l_f in Equation 11) of $l_f = 400$ m, a temperature difference of $\Delta T = 2.1°C$, and minimal noise $\sigma_n = 0.01$. The transect depths were set to $depths = [10, 20, 30, 40, 50]$ m, in order to mimic the desired depths of the field trials.

The estimated gradient along each transect is plotted in Figure 4, where the point of the maximum absolute value is indicated by a star. From Figures 3 and 4, we see that the front location is estimated to be located West of the initial transect. The consecutive transect is then moved West by the algorithm, and the front is contained in the latter three transects.

3.2   Field Trials

In the field trials, the goal was to prove the efficacy of the algorithm and thus gather relevant data; replicating the same set of depths as in the simulation trials, with a transect length of 5 km. Due to an unrelated error, the mission had to be restarted after the transect at 20 m and this is observable in Figure 5 (top), where the 10m and 30 m transects are in the same Latitude, even though the best estimate of the front position from the previous, 20 m, transect is further North. After the transect at 30 m, the mission had to be aborted due to a leak in the vehicle. Nevertheless, the data collected are sufficient to report and discuss the application of the front detection algorithm. The data is also plotted as a temperature field in Figure 5 (bottom), using a Gaussian process (GP) (Rasmussen, 2003; Cressie and Wikle, 2015). The temperature data was gridded
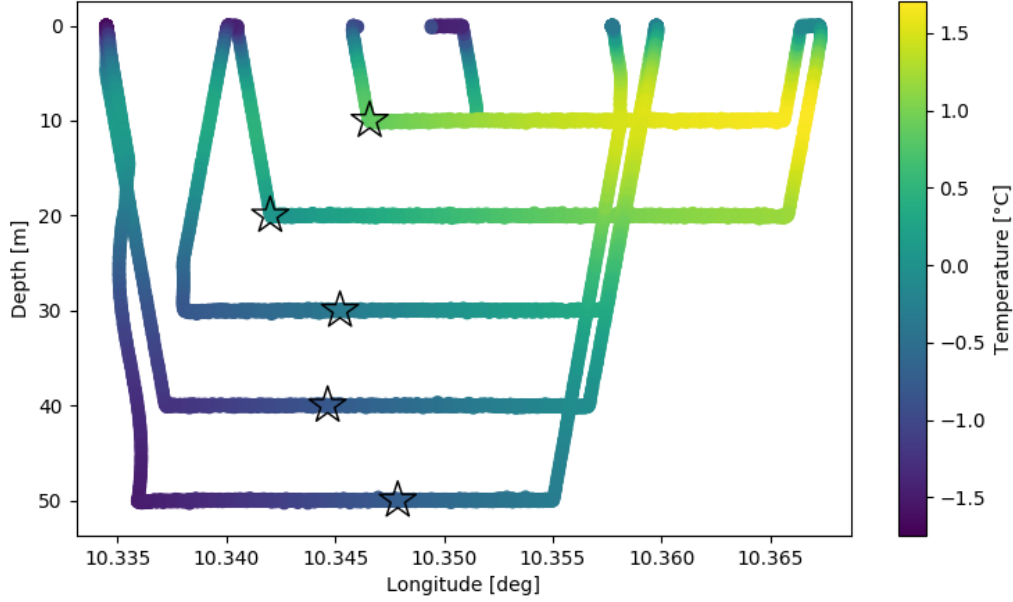
Figure 3: Transect across a simulated front at $depths = [10, 20, 30, 40, 50]$ m. Temperature is indicated by the color bar while the position of maximal absolute value of the estimated gradient is indicated by a star. The horizontal extent of each transect is about 400 m. The estimated front location is calculated after each surfacing event and the next transect is moved accordingly.

in a [lat,depth] grid, and the white circles in the figure indicate the grid points that contained data used for the GP. The length scales, nugget variance, and data variance were found by semivariogram. The GP was evaluated with a nugget variance of $\sigma^2_{nugget} = 0.03°\text{C}^2$, data variance of $\sigma^2_{data} = 0.27°\text{C}^2$ and a squared exponential kernel. The nugget variance represents both process and measurement noise, and is the variance between adjacent grid cells containing data. The length scales in the depth direction was set to 5.77m, and 0.0115°, which is equivalent to 1278 m, in the longitude-direction. The isothermal layers in the figure are more closely spaced near the surface and around the indicators of the front location, as opposed to the more homogeneous fields further North and South. In Figure 6, the differentiated NCSR and estimated front locations are plotted. The gradient is almost always negative, except for a small portion in the 10 m transect. The estimated front location displays high spatial correlation, and the magnitude of the gradient reduces with depth. This can indicate that the front is sharpest nearer the surface, and more diffuse at greater depths.

Microstructure measurements were sampled continuously during the three transects conducted by the LAUV. Figure 7 shows the time series of temperature and dissipation rate of turbulent kinetic energy estimated from the shear measurements during the transects. The dissipation rate systematically decrease with increased depth, as is expected in the surface boundary layer. In addition, the transects at 10 and 20 m suggest there is a relationship between the temperature gradient and the dissipation rate, larger gradients suggest larger dissipation rates. However, this relationship needs further investigation and is beyond the scope of this paper.

3.3   Algorithm performance

In both the simulated and field trials, the prior or deployment site is offset from the first estimate of the front location by some distance, such that the first estimated front location is at the end of the transect.
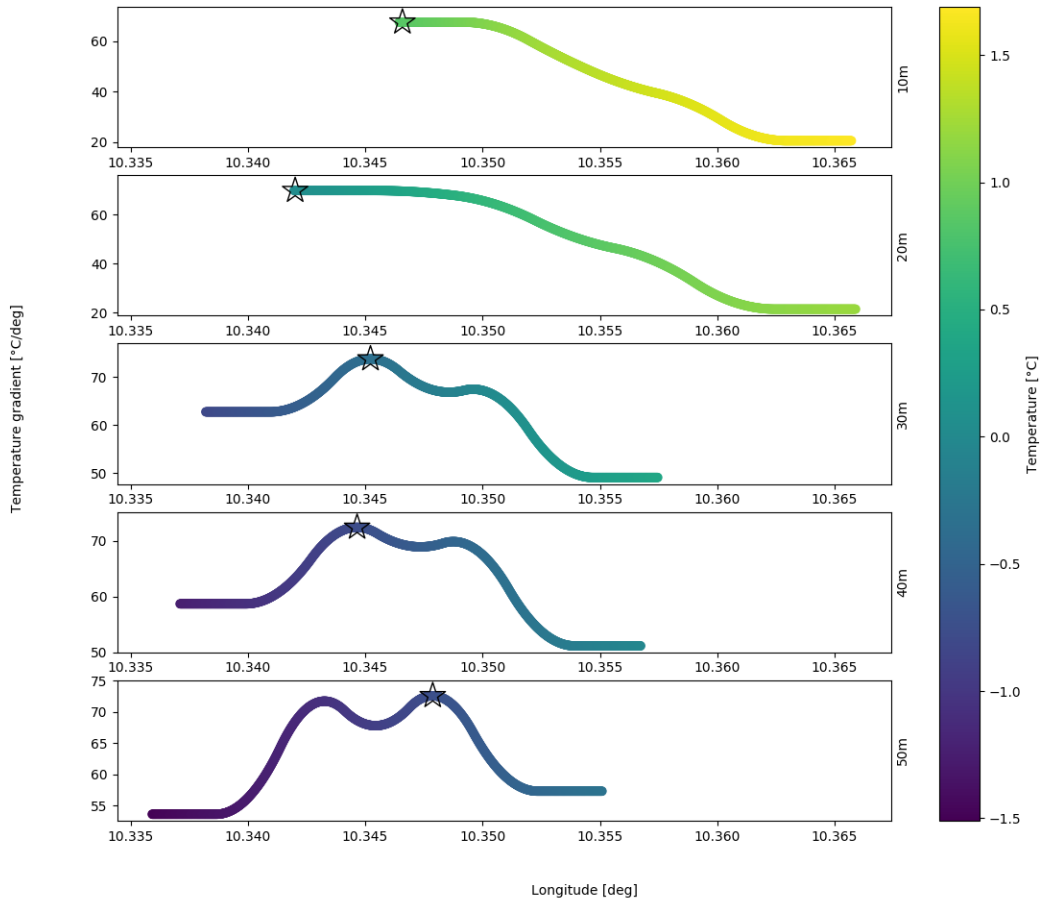
Figure 4: Transect across a simulated front at $depths = [10, 20, 30, 40, 50]$ m. Temperature is indicated by the color bar while the estimated gradient is plotted on the y-axis, and the position of maximal absolute value of the estimated gradient is indicated by a star.
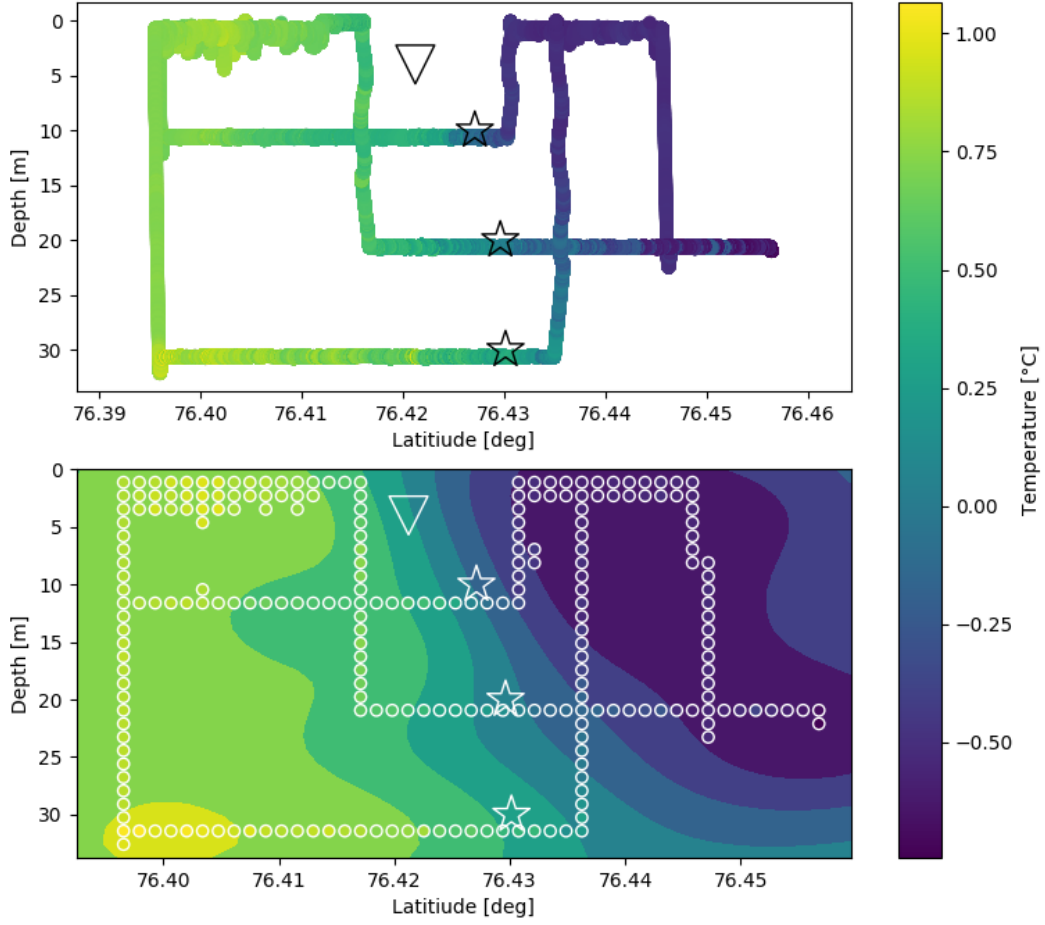
Figure 5: Transect across a polar front at 76° North, at $depths = [10, 20, 30]$m with temperature measurements in the top plot and estimated temperature field in the bottom plot represented by color. The estimate is generated by a Gaussian Process regression over the temperature data from the LAUV. The white circles indicate the locations of data projected on the evaluation grid, while the estimated position of maximal absolute value of the gradient is indicated by stars, and the initial estimate of the front location at 4 m from shipboard measurements is marked with a triangle.
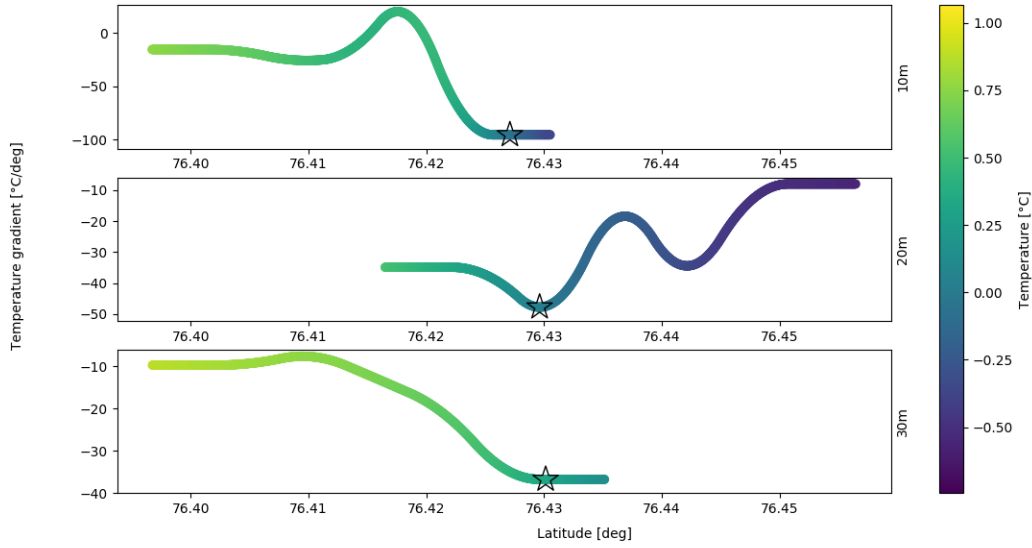
Figure 6: Transect across a polar front at $depths = [10, 20, 30]$ m, temperature is indicated by the color bar while the estimated gradient is plotted on the y-axis, and the position of maximal absolute value of the estimated gradient is indicated by a star. Note that the position of the front is estimated to be located at the gradient minima, which is the maximum absolute value.
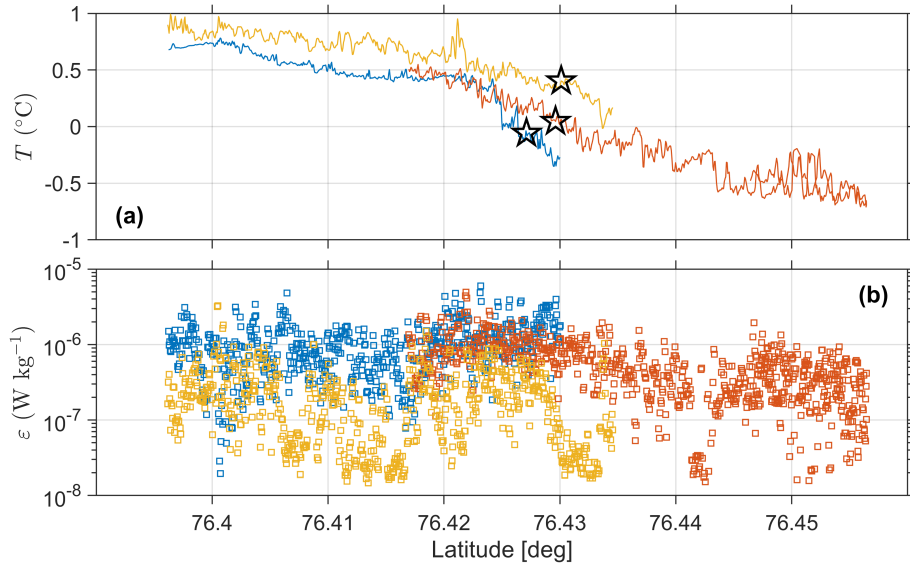

Figure 7: Overview of **a)** temperature, and **b)** the final estimate of the dissipation rate of turbulent kinetic energy, ε, plotted against latitude. Blue, red and yellow corresponds to 10, 20 and 30 m depth respectively. Stars indicate the location of the maximum absolute value of the estimated temperature gradient.

In the case of the field results, the end is the southernmost estimate of the maximum gradient value; the gradient is constant at the ends and the location of the maximum value is allocated to the first of the points of equal value, sorted South to North. In the simulation, the front location was estimated five times, and in the field trials three times; after each surfacing event. In all cases except for after the 20 m dive in the field trials, the estimate was used to place the next transect towards the site of the maximal absolute value of the gradient.

4   Discussion

By adapting the mission to the location of the maximum gradient we were able to measure dissipation rates horizontally across the polar front. This enables the study of heat exchange and mixing effects across the front, and the impacts of the two water masses on each other. Understanding the heat exchange between water masses and turbulent mixing processes is pivotal for the estimation of heat transport into the Arctic ocean.

4.1   Front location

The estimated position of the front, marked by stars in Figures 5 and 6, appears to be aligned in the North-direction. This might be an artifact, due to the clamping of the NCSR at the ends, by requiring the double derivative to vanish at the ends, leading the differentiated regression to be constant in each end. The maximum gradient is therefore along a segment of the regression, rather than a point. However, the placement of the maximum absolute value of the gradient in the North end of the transect is correct, and will push the next transect northwards, as it did from the 10 m depth transect to the 20 m depth transect. Note that the gradient is negative due to decreasing temperatures towards North.

As seen from the simulations and field trials, the maximum gradient along each transect is correctly identified. However, we see that the 10 m depth and 20 m depth transects in Figure 3 do not cross the position of maximal gradient. This could be circumvented by adding a threshold value check to the transect, such that the transect is guaranteed to cross that threshold. We see the same effect in the 30 m depth transect in Figure 6 and 7, where a steeper gradient is visible further north, but the detection is limited by the clamping of the second derivative near the ends of the NCSR, as seen by the flat ends of gradient estimates in Figures 4 and 6. This can be remedied by adding a higher resolution of knots near the ends, or checking if there is several positions that have the maximum gradient, and averaging them.

From the temperature transects in Figures 5 and 7a, we argue that the choice of six knots in the NCSR, $n_k = 6$, is sufficient for filtering out process and sensor noise. We are able to identify the maximal gradient in the correct scale, and thus adjust the AUV path. There can also be a case where the front is entirely missed, and the maximum gradient is incorrectly identified as the front. By adding a threshold value for the gradient, we could reject the estimate. Thereafter, we could attempt to regain the front by measures presented in Fossum et al. (2021a), or to stop the mission and ask for human intervention. As we target to measure dissipation rates across a temperature gradient, the main goal is to track the largest temperature gradients and not specific values.

4.2   Turbulence measurements

The dissipation rates measured across the front augment the vertical profiles taken from ship-borne platforms. This enables a more synoptic sampling for exploring the horizontal distribution of dissipation rates. Due to vehicle-induced noise, low dissipation rates are not detectable, but higher rates such as found in the upper 50 m and in frontal regions can be captured. The vibrations of the AUV, particularly those from the thruster, contaminate the shear probe records. Yet, by removing noise coherent with accelerometers on the MR, the shear signal is sufficiently cleaned for dissipation levels above 5×10^{-8} W kg^{-1}. The capability and the

limitations of the system for turbulence measurements are presented and discussed in detail in Kolås et al. (2022).

Dissipation rates measured from the AUV agree well with the measurements using a loosely-tethered vertical microstructure profiler from the ship (not shown). Our setup cannot detect dissipation rates below 5×10^{-8} W kg^{-1} reliably, and is unfit for use in quiescent boundary layers (Kolås et al., 2022). However, an improved installation of the turbulence probes on the nose of the AUV could potentially reduce some of the noise in the shear measurements, allowing acceptable quality dissipation measurements from the AUV also in relatively quiescent environments. For the scope of this method, the signal to noise ratio is acceptable.

4.3 Other use cases

It might be tempting to generalize this method for use on other autonomous or remotely-piloted ocean robots such as gliders and surface vehicles. As gliders follow a yoyo-pattern of flight, they collect data along a slanted path. The horizontal and vertical variations mixed in the data would be difficult to untangle, thus making the front detection method not suitable for gliders, at least over short distances. Adjustments in the method and the algorithm could allow for applications in underwater gliders, which would improve the efficiency of targeted sampling considerably, while allowing for longer transects needed to sufficiently cover both sides of ocean fronts. If one were to implement the algorithm on a surface vehicle, then one could traverse the front in a lawnmower-pattern, adjusting each transect based on the previous ones. Finally, one could use the method directly on any towed sensor where the depth is adjustable.

For an open ocean front system, the transect length could have been longer (Rossby radius of deformation is typically 5 to 10 km). However this would reduce the number of front crossings per unit of time. Longer transects will require using a vehicle with greater endurance. As a feature, temperature can be exchanged for salinity, chlorophyll-a or any other relevant record available in real time from the on board sensors.

5 Conclusion and further work

We have presented a method using the maximum horizontal temperature gradient as the input for adaptive mission planning. We found and tracked a maximum horizontal gradient point within an oceanic front using an AUV for the purpose of microstructure measurements. The method is tested in the field and allowed successful collection of targeted data on the polar front in the Barents Sea. We were able to detect and follow the maximum horizontal temperature gradient, capturing hydrographic and microstructure data at the front and on both warm and cold sides of the front. For future implementations, we recommend adding a threshold value of the maximum gradient in case the true front is not crossed and detected.

References

Belkin, I. M., Cornillon, P. C., and Sherman, K. (2009). Fronts in large marine ecosystems. *Progress in Oceanography*, 81(1-4):223–236.

Cressie, N. and Wikle, C. K. (2015). *Statistics for spatio-temporal data*. John Wiley & Sons.

D'Asaro, E., Lee, C., Rainville, L., Harcourt, R., and Thomas, L. (2011). Enhanced turbulence and energy dissipation at ocean fronts. *science*, 332(6027):318–322.

Fer, I., Mo-Bjørkelund, T., and Kolås, E. H. (2021). Dissipation measurements from AUV transects across a surface temperature front in the Barents Sea.

Fer, I., Peterson, A. K., and Ullgren, J. E. (2014). Microstructure measurements from an underwater glider in the turbulent faroe bank channel overflow. *Journal of Atmospheric and Oceanic Technology*, 31(5):1128–1150.

Fossum, T. O. (2019). *Adaptive Sampling for Marine Robotics*. PhD thesis, Norwegian University of Science and Technology.

Fossum, T. O., Eidsvik, J., Ellingsen, I., Alver, M. O., Fragoso, G. M., Johnsen, G., Mendes, R., Ludvigsen, M., and Rajan, K. (2018). Information-driven robotic sampling in the coastal ocean. *Journal of Field Robotics*, 35(7):1101–1121.

Fossum, T. O., Fragoso, G. M., Davies, E. J., Ullgren, J. E., Mendes, R., Johnsen, G., Ellingsen, I., Eidsvik, J., Ludvigsen, M., and Rajan, K. (2019). Toward adaptive robotic sampling of phytoplankton in the coastal ocean. *Science Robotics*, 4(27).

Fossum, T. O., Norgren, P., Fer, I., Nilsen, F., Koenig, Z. C., and Ludvigsen, M. (2021a). Adaptive sampling of surface fronts in the arctic using an autonomous underwater vehicle. *IEEE Journal of Oceanic Engineering*.

Fossum, T. O., Travelletti, C., Eidsvik, J., Ginsbourger, D., and Rajan, K. (2021b). Learning excursion sets of vector-valued gaussian random fields for autonomous ocean sampling. *The Annals of Applied Statistics*, 15(2):597–618.

Garabato, A. C. N., Frajka-Williams, E. E., Spingys, C. P., Legg, S., Polzin, K. L., Forryan, A., Abrahamsen, E. P., Buckingham, C. E., Griffies, S. M., McPhail, S. D., et al. (2019). Rapid mixing and exchange of deep-ocean waters in an abyssal boundary current. *Proceedings of the National Academy of Sciences*, 116(27):13233–13238.

Gawarkiewicz, G. and Plueddemann, A. J. (1995). Topographic control of thermohaline frontal structure in the Barents Sea Polar Front on the south flank of Spitsbergen Bank. *Journal of Geophysical Research*, 100(C3):4509.

Goodman, L., Levine, E. R., and Lueck, R. G. (2006). On measuring the terms of the turbulent kinetic energy budget from an auv. *Journal of Atmospheric and Oceanic Technology*, 23(7):977–990.

Jakobsson, M., Mayer, L. A., Bringensparr, C., Castro, C. F., Mohammad, R., Johnson, P., Ketter, T., Accettella, D., Amblas, D., An, L., Arndt, J. E., Canals, M., Casamor, J. L., Chauché, N., Coakley, B., Danielson, S., Demarte, M., Dickson, M.-L., Dorschel, B., Dowdeswell, J. A., Dreutter, S., Fremand, A. C., Gallant, D., Hall, J. K., Hehemann, L., Hodnesdal, H., Hong, J., Ivaldi, R., Kane, E., Klaucke, I., Krawczyk, D. W., Kristoffersen, Y., Kuipers, B. R., Millan, R., Masetti, G., Morlighem, M., Noormets, R., Prescott, M. M., Rebesco, M., Rignot, E., Semiletov, I., Tate, A. J., Travaglini, P., Velicogna, I., Weatherall, P., Weinrebe, W., Willis, J. K., Wood, M., Zarayskaya, Y., Zhang, T., Zimmermann, M., and Zinglersen, K. B. (2020). The International Bathymetric Chart of the Arctic Ocean Version 4.0. *Scientific Data*, 7(1):176.

Kolås, E. H., Mo-Bjørkelund, T., and Fer, I. (2022). Technical note: Turbulence measurements from a light autonomous underwater vehicle. *Ocean Science*, 18(2):389–400.

McGann, C., Py, F., Rajan, K., Thomas, H., Henthorn, R., and Mcewen, R. (2008). A deliberative architecture for auv control. In *2008 IEEE International Conference on Robotics and Automation*, pages 1049–1054. IEEE.

Merckelbach, L., Berger, A., Krahmann, G., Dengler, M., and Carpenter, J. R. (2019). A dynamic flight model for slocum gliders and implications for turbulence microstructure measurements. *Journal of Atmospheric and Oceanic Technology*, 36(2):281–296.

Mo-Bjørkelund, T., Fossum, T. O., Norgren, P., and Ludvigsen, M. (2020). Hexagonal grid graph as a basis for adaptive sampling of ocean gradients using auvs. In *Global Oceans 2020: Singapore–US Gulf Coast*, pages 1–5. IEEE.

Nilsen, F., Fer, I., Baumann, T. M., Breivik, Ø., Czyz, C., Frank, L., Kalhagen, K., Koenig, Z., Kolås, E. H., Kral, S. T., et al. (2021). Pc-2 winter process cruise (wpc): Cruise report. *The Nansen Legacy Report Series*, 1(26).

Osborn, T. and Crawford, W. (1980). An airfoil probe for measuring turbulent velocity fluctuations in water. In *Air-Sea Interaction*, pages 369–386. Springer.

OSI SAF (2017). Global Sea Ice Concentration (netCDF) - DMSP.

Oziel, L., Sirven, J., and Gascard, J.-C. (2016). The Barents Sea frontal zones and water masses variability (1980–2011). *Ocean Science*, 12(1):169–184.

Parsons, A. R., Bourke, R. H., Muench, R. D., Chiu, C.-S., Lynch, J. F., Miller, J. H., Plueddemann, A. J., and Pawlowicz, R. (1996). The Barents Sea Polar Front in summer. *Journal of Geophysical Research: Oceans*, 101(C6):14201–14221.

Pinto, J., Mendes, R., da Silva, J. C., Dias, J. M., and de Sousa, J. B. (2018). Multiple autonomous vehicles applied to plume detection and tracking. In *2018 OCEANS-MTS/IEEE Kobe Techno-Oceans (OTO)*, pages 1–6. IEEE.

Quigley, M., Conley, K., Gerkey, B., Faust, J., Foote, T., Leibs, J., Wheeler, R., and Ng, A. Y. (2009). Ros: an open-source robot operating system. In *ICRA workshop on open source software*, page 5. Kobe, Japan.

Rasmussen, C. E. (2003). Gaussian processes in machine learning. In *Summer School on Machine Learning*, pages 63–71. Springer.

Seto, M. L. (2012). *Marine robot autonomy*. Springer Science & Business Media.

Sousa, A., Madureira, L., Coelho, J., Pinto, J., Pereira, J., Sousa, J. B., and Dias, P. (2012). Lauv: The man-portable autonomous underwater vehicle. *IFAC Proceedings Volumes*, 45(5):268–274.

Spingys, C. P., Naveira Garabato, A. C., Legg, S., Polzin, K. L., Abrahamsen, E. P., Buckingham, C. E., Forryan, A., and Frajka-Williams, E. E. (2021). Mixing and transformation in a deep western boundary current: A case study. *Journal of Physical Oceanography*, 51(4):1205–1222.

Stankiewicz, P., Tan, Y. T., and Kobilarov, M. (2021). Adaptive sampling with an autonomous underwater vehicle in static marine environments. *Journal of Field Robotics*, 38(4):572–597.

Wolk, F., Lueck, R., and Laurent, L. S. (2009a). Turbulence measurements from a glider. In *OCEANS 2009*, pages 1–6. IEEE.

Wolk, F., Lueck, R. G., and St. Laurent, L. (2009b). Turbulence measurements from a glider. In *OCEANS 2009*, pages 1–6.

Zhang, Y., Bellingham, J. G., Ryan, J. P., Kieft, B., and Stanway, M. J. (2013). Two-dimensional mapping and tracking of a coastal upwelling front by an autonomous underwater vehicle. In *2013 OCEANS-San Diego*, pages 1–4. IEEE.

Zhang, Y., Bellingham, J. G., Ryan, J. P., Kieft, B., and Stanway, M. J. (2016). Autonomous four-dimensional mapping and tracking of a coastal upwelling front by an autonomous underwater vehicle. *Journal of Field Robotics*, 33(1):67–81.

Zhang, Y., Kieft, B., Hobson, B. W., Ryan, J. P., Barone, B., Preston, C. M., Roman, B., Raanan, B.-Y., Marin III, R., O'Reilly, T. C., et al. (2019). Autonomous tracking and sampling of the deep chlorophyll maximum layer in an open-ocean eddy by a long-range autonomous underwater vehicle. *IEEE Journal of Oceanic Engineering*.

Zhang, Y., Ryan, J. P., Bellingham, J. G., Harvey, J. B., and McEwen, R. S. (2012). Autonomous detection and sampling of water types and fronts in a coastal upwelling system by an autonomous underwater vehicle. *Limnology and Oceanography: Methods*, 10(11):934–951.